



Cite this: *RSC Adv.*, 2025, **15**, 42594

Interplay of matrix porosity and phase interfaces in lithium-ion transport of Sn–CS nanocomposites

Rana Said,^a Shaker Al-Hasnaawi,^{bc} M. M. Rekha,^d Subhashree Ray,^e Kattela Chennakesavulu,^f Vipasha Sharma^g and Arsham Banimadadi  

Tin–carbon–silica (Sn–CS) nanocomposites are promising anode materials for lithium-ion batteries owing to their high theoretical capacity and structural stability. However, their performance is critically influenced by matrix porosity and interfacial transport barriers. In this work, a three-dimensional multiphysics model was developed to elucidate lithium-ion diffusion and charge transport across tin, carbon, and silica phases. The simulations reveal that an intermediate porosity of ~40% offers the best balance between ionic mobility and structural integrity, while excessive porosity disrupts electronic pathways and low porosity limits electrolyte infiltration. Phase-resolved analysis highlights tin as the most efficient diffusion medium, whereas silica interfaces create significant bottlenecks that induce steep lithium concentration gradients and up to 20% capacity loss at high charge rates. Model validation against experimental data confirms the accuracy of the predictions. These findings demonstrate that tuning porosity and interfacial architecture can effectively mitigate diffusion limitations, providing a rational design strategy for next-generation Sn-based nanocomposites. Beyond anodes, the presented multiphysics approach offers a generalizable framework for understanding and optimizing transport processes in multifunctional nanostructured materials.

Received 9th September 2025
 Accepted 22nd October 2025

DOI: 10.1039/d5ra06813d
rsc.li/rsc-advances

1. Introduction

Lithium-ion batteries (LIBs) are at the forefront of electrochemical energy storage, powering a broad range of technologies from consumer electronics to electric vehicles and grid applications.^{1–3} Their success is driven by high energy density, long cycle life, and high coulombic efficiency. However, the increasing demand for fast-charging, high-capacity, and long-lasting LIBs highlights critical limitations in conventional graphite anodes, which offer a theoretical capacity of only 372 mAh g^{−1} and limited rate capability.^{4,5} These limitations have prompted intensive research into alternative high-capacity anode materials.

^aFaculty of Pharmacy, Hourani Center for Applied Scientific Research, Al-Ahliyya Amman University, Amman, Jordan

^bCollege of Pharmacy, The Islamic University, Najaf, Iraq

^cDepartment of Medical Analysis, Medical Laboratory Technique College, The Islamic University of Al Diwaniyah, Al Diwaniyah, Iraq

^dDepartment of Chemistry and Biochemistry, School of Sciences, JAIN (Deemed to be University), Bangalore, Karnataka, India

^eDepartment of Biochemistry, IMS and SUM Hospital, Siksha 'O' Anusandhan, Bhubaneswar, Odisha-751003, India

^fDepartment of Chemistry, Sathyabama Institute of Science and Technology, Chennai, Tamil Nadu, India

^gDepartment of Biotechnology, University Institute of Biotechnology, Chandigarh University, Mohali, Punjab, India

^hYoung Researchers and Elite Club, Tehran University, Tehran, Iran. E-mail: arshambanimadadi.academic@gmail.com

Among various candidates, tin (Sn) has emerged as a promising anode material due to its high theoretical capacity of 994 mAh g^{−1}, which arises from the formation of lithium-rich intermetallic phases (e.g., Li_{4.4}Sn) during lithiation.^{6–8} However, the commercial adoption of Sn-based anodes is hindered by substantial volume changes (>260%) during lithiation/delithiation cycles, leading to pulverization, loss of electrical connectivity, and capacity fading.^{9–11} Embedding Sn nanoparticles within conductive and mechanically stable matrices such as carbon and silica has been proposed as a viable strategy to buffer volume expansion and improve cycling performance.^{12–14}

Sn-based nanocomposites combining carbon and silicon dioxide (Sn–CS) represent a hybrid architecture designed to leverage the high conductivity of carbon, the mechanical buffering of silica, and the electrochemical activity of tin.^{15–17} In this composite, carbon facilitates electronic conductivity and limited lithium intercalation, tin provides alloying capability with lithium, and silica contributes to mechanical integrity while impeding excessive volumetric changes.^{18,19} Despite these advantages, a key limitation lies in the inherently poor lithium-ion conductivity of silica and the non-uniform phase interfaces, which introduce diffusion bottlenecks and restrict rate capability.^{20,21}

Porosity in Sn–CS nanocomposites plays a pivotal role in enhancing lithium-ion transport by reducing tortuosity and improving electrolyte infiltration.²² At the same time, excessive



porosity can compromise structural strength and disrupt electronic percolation networks.^{23,24} Therefore, optimizing porosity is essential to balance transport and mechanical performance. Several studies have shown that moderate porosity levels (~40%) often yield the best compromise between diffusivity and structural integrity.^{25–27}

In multiphase systems such as Sn–CS, phase-specific diffusion strongly influences overall battery performance. Tin offers fast lithium transport due to its metallic structure and high lithium solubility.²⁸ In contrast, amorphous carbon presents moderate lithium diffusivity, while silica remains nearly inactive due to its dense covalent structure and high dielectric constant.^{29,30} As a result, significant lithium concentration gradients can develop at the tin–carbon and carbon–silica interfaces during high-rate operation,³¹ which degrade active material utilization and limit capacity retention.

Conventional experimental techniques such as electrochemical impedance spectroscopy or cyclic voltammetry provide indirect insights into ion transport properties. However, these methods fall short in resolving localized phenomena at the nanoscale. To overcome these limitations, computational modeling has become increasingly important for evaluating electrochemical and transport behaviors in heterogeneous materials.^{32–34}

COMSOL Multiphysics is a powerful finite element-based simulation platform widely adopted in electrochemical engineering for its ability to solve coupled transport, electrochemical, and structural equations in complex geometries.³⁵ Specifically, its Transport of Diluted Species and Electric Currents modules allow detailed modeling of lithium-ion diffusion and charge transfer in porous and multiphase electrodes. By implementing custom-defined material parameters (such as phase-dependent diffusion coefficients, porosity, and tortuosity) COMSOL enables realistic simulation of lithium-ion transport in nanostructured composites. Its 3D modeling capabilities, combined with advanced meshing and solver tools, make it particularly suitable for analyzing phase interactions and interface effects in systems.^{36,37} Moreover, COMSOL's flexibility allows researchers to simulate time-dependent charge/discharge cycles and extract spatial concentration profiles, fluxes, and electrochemical performance metrics.

The novelty of this work lies in its comprehensive multiphysics modeling approach that simultaneously accounts for matrix porosity, phase-specific diffusion coefficients, and charge-rate effects within Sn–CS nanocomposites. Despite extensive efforts to improve Sn-based anodes through nanostructuring and composite design, most previous studies have focused either on experimental synthesis or on simplified electrochemical modeling.^{38–40} While these approaches have provided valuable insights into cycling stability and capacity retention, they often lack a detailed, phase-resolved understanding of lithium-ion transport at the nanoscale. In particular, the combined effects of matrix porosity, phase-specific diffusion coefficients, and interfacial transport resistances have not been systematically investigated using fully three-dimensional multiphysics simulations validated against experimental data. This knowledge gap limits the rational design of

Sn–CS nanocomposites, as it remains unclear how porosity tuning and phase distribution collectively influence lithium diffusion and high-rate performance.

To address this gap, the present study develops a comprehensive 3D multiphysics model of Sn–CS nanocomposites, explicitly incorporating porosity-dependent transport, Butler–Volmer kinetics, and phase-specific diffusion behavior. By validating the model against experimental results, we demonstrate how an optimized porosity of ~40% can simultaneously enhance lithium-ion mobility and maintain structural robustness. This work provides mechanistic insights that bridge the gap between experimental observations and theoretical predictions, offering a practical framework for the rational design of high-performance Sn-based anodes.

2. Methodology

2.1. Parameters

The tin-embedded carbon/silica (Sn–CS) nanocomposite was modeled with specific material and electrochemical parameters to ensure accurate simulation of lithium-ion transport. The diffusion coefficients for each phase were carefully selected based on experimental and computational studies relevant to the Sn–CS system. For tin, a diffusion coefficient of $D_{\text{Sn}} = 1.00 \times 10^{-9} \text{ cm}^2 \text{ s}^{-1}$ was used, consistent with its metallic nature and high lithium solubility.⁴¹ For amorphous carbon, a diffusion coefficient of $D_c = 1.00 \times 10^{-11} \text{ cm}^2 \text{ s}^{-1}$ was adopted, aligning with reported values for disordered carbon structures (e.g., mesocarbon microbeads, artificial graphite) which typically range from 10^{-10} to $10^{-12} \text{ cm}^2 \text{ s}^{-1}$, as measured by galvanostatic intermittent titration technique (GITT) and electrochemical impedance spectroscopy (EIS).^{42,43} For silica (SiO_2), a diffusion coefficient of $D_{\text{SiO}_2} = 1.00 \times 10^{-13} \text{ cm}^2 \text{ s}^{-1}$ was selected, reflecting its insulating covalent network that imposes high energy barriers for lithium-ion migration, with literature values ranging from 10^{-13} to $10^{-16} \text{ cm}^2 \text{ s}^{-1}$ based on first-principles calculations.⁴⁴

These values account for the morphological and structural characteristics of the Sn–CS nanocomposite, ensuring reliable simulation of phase-specific transport. Table 1 summarizes these parameters, detailing diffusion coefficients, electrical conductivities, tortuosity relations, electrochemical constants, and geometric specifications used in the COMSOL Multiphysics simulations. Each row corresponds to a specific parameter, categorized by phase (tin, carbon, silica, electrolyte) or system property (e.g., tortuosity, geometry), with values sourced from ref. 41 unless otherwise noted. The table structure is designed to provide a comprehensive overview of inputs for the multiphysics model. All parameter fields were fully defined to ensure reproducibility and consistency. Model included tin nanoparticles (diameter: 10 nm) embedded in a carbon–silica matrix with porosity levels of 20%, 40%, and 60%.

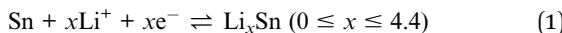
2.2. Reactions

The primary electrochemical reaction in the Sn–CS nanocomposite involves lithium alloying with tin, described as:

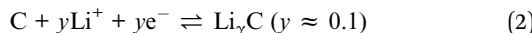


Table 1 Material and electrochemical parameters of Sn–CS nanocomposite⁴¹

Parameter	Material	Value	Unit
Diffusion coefficient	Tin (Sn)	$D_{\text{Sn}} = 1.00 \times 10^{-9}$	$\text{cm}^2 \text{ s}^{-1}$
	Carbon (C)	$D_c = 1.00 \times 10^{-11}$	$\text{cm}^2 \text{ s}^{-1}$
	Silica (SiO_2)	$D_{\text{SiO}_2} = 1.00 \times 10^{-13}$	$\text{cm}^2 \text{ s}^{-1}$
Electrical conductivity	Electrolyte	$D_{\text{Electrolyte}} = 7.5 \times 10^{-9}$	$\text{cm}^2 \text{ s}^{-1}$
	Carbon (C)	$\sigma_c = 100$	S m^{-1}
	Silica (SiO_2)	$\sigma_{\text{SiO}_2} = 1.0 \times 10^{-14}$	S m^{-1}
Tortuosity relation	Tin (Sn)	$\sigma_{\text{Sn}} = 1.0 \times 10^7$	S m^{-1}
	—	$\tau = \varepsilon^{-0.5}$	—
	—	$j_0 = 0.01$	mA cm^{-2}
Electrochemical	Exchange current density	$\alpha = 0.5$	—
	Transfer coefficient	$T = 298$	K
	Temperature	$F = 96\,485$	C mol^{-1}
	Faraday constant	$R = 8.314$	$\text{J mol}^{-1} \text{ K}^{-1}$
	Gas constant	50	μm
	Electrode thickness	1	μm
	Electrolyte layer	$100 \times 100 \times 100$	nm^3
Geometry	RVE size		



This reaction forms lithium–tin alloys, contributing to high lithium storage capacity. The carbon phase supports limited lithium intercalation.⁴⁵



Silica (SiO_2) is electrochemically inactive but influences ion transport due to its insulating nature.

2.3. Governing equations

The simulation of lithium-ion transport and electrochemical behavior in the tin-embedded carbon/silica (Sn–CS) nanocomposite was governed by a set of coupled partial differential equations, implemented in COMSOL Multiphysics to model diffusion and electrochemical kinetics across the tin, carbon, and silica phases, as well as the electrode–electrolyte interface.

2.4. Lithium-ion diffusion

Lithium-ion transport in each phase (tin, carbon, silica, and electrolyte) was modeled using Fick's second law of diffusion, expressed as:⁴⁶

$$\frac{\partial C_i}{\partial t} = \nabla \cdot (D_i \nabla C_i) \quad (3)$$

where C_i (mol m^{-3}) is the lithium-ion concentration in phase i , D_i ($\text{cm}^2 \text{ s}^{-1}$) is the diffusion coefficient for phase i , with values: $D_{\text{Sn}} = 1.00 \times 10^{-9}$, $D_c = 1.00 \times 10^{-11}$, $D_{\text{SiO}_2} = 1.00 \times 10^{-13}$, and $D_{\text{Electrolyte}} = 7.5 \times 10^{-9}$.

For the porous carbon–silica matrix, the effective diffusion coefficient (D_{eff}) was adjusted to account for porosity (ε) and tortuosity (τ) using the Bruggeman relation:⁴⁷

$$D_{\text{eff}} = D_{\text{matrix}} \times \varepsilon^{1.5} \quad (4)$$

where D_{matrix} is the intrinsic diffusion coefficient of the carbon–silica composite, calculated as a volume-weighted average of carbon and silica diffusion coefficients:⁴⁸

$$D_{\text{matrix}} = f_c \times D_c + f_{\text{SiO}_2} \times D_{\text{SiO}_2} \quad (5)$$

With f_c and f_{SiO_2} as the volume fractions of carbon and silica, respectively.

2.5. Electrochemical kinetics

The electrochemical reaction at the electrode–electrolyte interface, primarily lithium alloying with tin, was modeled using the Butler–Volmer equation to describe the current density:⁴⁹

$$j = j_0 \times [\exp((\alpha F\eta)/(RT)) - \exp(-(1 - \alpha)F\eta/(RT))] \quad (6)$$

where j (A m^{-2}) is the current density, $j_0 = 0.01 \text{ mA cm}^{-2}$ is the exchange current density, $\alpha = 0.5$ is the charge transfer coefficient, $F = 96\,485 \text{ C mol}^{-1}$ is Faraday's constant, $\eta = \varphi_s - \varphi_e - E_{\text{eq}}$ (V) is the overpotential, φ_s and φ_e (V) are the solid and electrolyte potentials, E_{eq} (V) is the equilibrium potential of the tin–lithium alloying reaction, $R = 8.314 \text{ (J mol}^{-1} \text{ K}^{-1})$ is the gas constant and $T = 298 \text{ K}$ is the temperature.

The current density was coupled to the lithium-ion flux at the interface *via*:

$$N_i = -j/F \quad (7)$$

where N_i ($\text{mol m}^{-2} \text{ s}^{-1}$) is the molar flux of lithium ions.

2.6. Charge conservation

Charge transport in the solid (electrode) and electrolyte phases was governed by Ohm's law and charge conservation:⁵⁰

$$\nabla \cdot (\sigma_i \nabla \varphi_i) = 0 \quad (8)$$



where σ_i (S m^{-1}) is the electrical conductivity of phase i , with values: $\sigma_{\text{Sn}} = 10^7$, $\sigma_{\text{c}} = 100$, $\sigma_{\text{SiO}_2} = 10^{-14}$, $\sigma_{\text{electrolyte}} = 1 \text{ S m}^{-1}$, and φ_i (V) is the potential in phase i .

For the porous matrix, the effective conductivity was adjusted for porosity:⁵¹

$$\sigma_{\text{eff}} = \sigma_{\text{matrix}} \times \varepsilon^{1.5} \quad (9)$$

where σ_{matrix} is the intrinsic conductivity of the carbon–silica composite.

2.7. Interface conditions

At phase interfaces (tin–carbon, carbon–silica), continuity of lithium-ion concentration and flux was enforced:⁵²

$$C_i = C_j, D_i \cdot \nabla C_i, n = D_j \nabla C_j \cdot n \quad (10)$$

where n is the unit normal vector at the interface.

These equations collectively describe lithium-ion diffusion, electrochemical reactions, and charge transport, enabling accurate simulation of the Sn–CS nanocomposite's performance under varying porosity and charge rate conditions.

2.8. Simulation method

The simulations were conducted using the transport of diluted species and electric currents modules in COMSOL Multiphysics (version 6.2). A 3D RVE was constructed, with tin nanoparticles randomly distributed in a porous carbon–silica matrix. The model was discretized using a tetrahedral mesh with 12 000 elements, refined near phase interfaces to capture concentration gradients. A relative tolerance of 10^{-6} ensured numerical convergence.

2.9. Simulation implementation

The simulation of lithium-ion transport in the tin-embedded carbon/silica (Sn–CS) nanocomposite was performed using COMSOL Multiphysics with the transport of diluted species and electric currents modules. A three-dimensional (3D) representative volume element (RVE) of the Sn–CS nanocomposite was constructed. Three porosity levels (20%, 40%, and 60%) were modeled to assess their impact on lithium-ion diffusion, with tortuosity calculated using the Bruggeman relation:

$$\tau = \varepsilon^{-0.5} \quad (11)$$

The model was discretized using a tetrahedral mesh comprising 12 000 elements, with finer meshing near phase interfaces (tin–carbon and carbon–silica) to accurately capture concentration gradients. Mesh convergence was verified with a relative tolerance of 10^{-6} . The PARDISO direct solver was employed for solving the coupled diffusion and electrochemical equations, ensuring numerical stability and efficiency.

2.9.1. Initial conditions. At $t = 0$, the lithium-ion concentration was initialized to $C_0 = 0 \text{ mol m}^{-3}$ across all phases (tin, carbon, silica, and electrolyte) to represent a fully discharged state. The solid and electrolyte potentials were set to $\varphi_s = 0 \text{ V}$ and $\varphi_e = 0 \text{ V}$, respectively.

2.9.2. Boundary conditions. A constant lithium-ion flux was applied at the electrode–electrolyte interface, calculated by eqn (7), where j is the current density (0.1 mA cm^{-2} for 1C, 0.2 mA cm^{-2} for 2C) and $F = 96\,485 \text{ C mol}^{-1}$ is Faraday's constant. The current collector boundary was set to zero lithium-ion flux ($\nabla C \cdot n = 0$) to simulate an impermeable surface. The electrolyte boundary maintained a constant lithium concentration of $C_{\text{electrolyte}} = 1\,000 \text{ mol m}^{-3}$. Continuity of concentration and flux was enforced at tin–carbon and carbon–silica interfaces as:

$$C_i = C_j, D_i \nabla C_i, n = D_j \nabla C_j \cdot n \quad (12)$$

where n is the unit normal vector.

2.9.3. Implementation process. The simulation iteratively solved Fick's second law for lithium diffusion and the Butler–Volmer equation for electrochemical kinetics, coupled with charge conservation. Outputs included lithium concentration profiles, effective diffusion coefficients, and normalized capacity, calculated by integrating lithium uptake over the electrode volume. Post-processing involved extracting concentration gradients across phases and capacity retention relative to 1C, with results exported for visualization in line and bar graphs.

2.10. Model validation

To ensure the reliability of the simulation results for the tin-embedded carbon/silica (Sn–CS) nanocomposite, the model was validated against experimental data from the first-cycle voltage profile of the Sn-49-CS electrode measured at a current density of 45 mA g^{-1} (0.0–2.5 V vs. Li/Li⁺) as reported by Hwang *et al.*⁴¹ The experimental data provided voltage–capacity profiles for the Sn–CS anode at a 1C charge rate, which were compared with the simulated capacity derived from lithium-ion uptake in the model (Fig. 1). The simulated capacity was calculated by

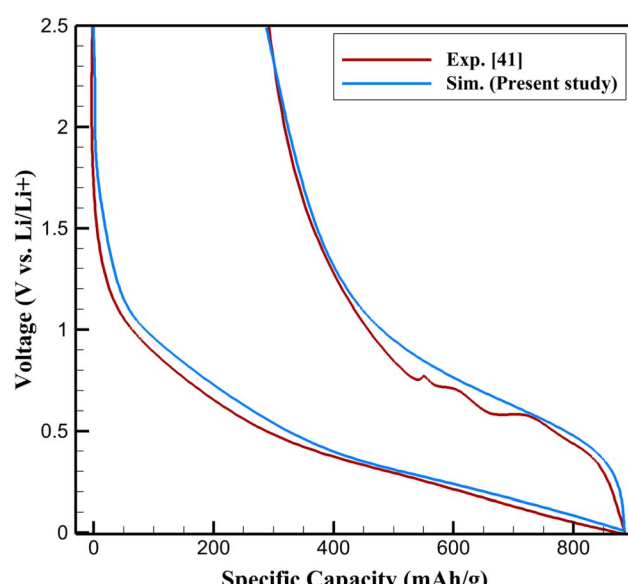


Fig. 1 Comparison between simulated and experimental voltage–capacity profiles of the Sn-49-CS electrode at the first cycle.



integrating the lithium concentration over the electrode volume at the end of charge cycle, using the transport of diluted species module in COMSOL Multiphysics.

The accuracy of the simulation was quantified using the Root Mean Square Error (RMSE) between the simulated and experimental capacity values across the voltage range (0.01–2.5 V). The RMSE was calculated as:

$$\text{RMSE} = \sqrt{\frac{1}{N} \sum_{i=1}^N (C_{\text{sim},i} - C_{\text{exp},i})^2} \quad (13)$$

where $C_{\text{sim},i}$ and $C_{\text{exp},i}$ are the simulated and experimental capacities at data point i , and N is the number of data points. The calculated RMSE was 0.23, indicating high accuracy and close agreement with the experimental data.

This low error suggests that the model effectively captures the lithium-ion diffusion and electrochemical kinetics of the Sn–CS nanocomposite, particularly the contributions of the tin phase's alloying reaction and the carbon–silica matrix's transport properties. Discrepancies may arise from unmodeled factors, such as minor side reactions or variations in experimental electrode morphology, but the RMSE of 0.23 confirms the model's robustness for predicting performance under varying porosity and charge rate conditions.

The voltage–capacity curve in Fig. 1 exhibits fluctuations, particularly in the experimental profile, which reflect the multi-step electrochemical reactions during the first lithiation cycle. These fluctuations primarily stem from the sequential formation of lithium–tin alloy phases (e.g., Li_2Sn_5 , LiSn , Li_7Sn_3 , up to $\text{Li}_{4.4}\text{Sn}$), each associated with distinct voltage plateaus due to varying Gibbs free energies of formation.⁴¹ The tin phase's high lithium solubility enables these phase transitions, causing stepwise voltage changes as lithium content increases. Additionally, minor contributions from lithium intercalation into the amorphous carbon phase (e.g., $\text{Li}_{0.1}\text{C}$) introduce subtle voltage variations, particularly at higher potentials. The simulated curve closely follows these trends, capturing the alloying stages, though slight smoothing occurs due to the model's continuum approach, which averages localized phase transformation effects. These fluctuations confirm the model's ability to represent the complex electrochemical behavior of the Sn–CS nanocomposite.

3. Results and discussion

3.1. Effect of matrix porosity on lithium-ion transport

The influence of matrix porosity on lithium-ion transport within the tin-embedded carbon/silica (Sn–CS) nanocomposite was investigated using COMSOL Multiphysics, focusing on its implications for lithium-ion battery anode performance. Three porosity levels (20%, 40%, and 60%) were modeled to assess their impact on lithium-ion diffusion in the carbon–silica matrix (Fig. 2). The effective diffusion coefficient (D_{eff}) was calculated using Fick's second law:

$$\frac{\partial C}{\partial t} = D_{\text{eff}} \nabla^2 C \quad (14)$$

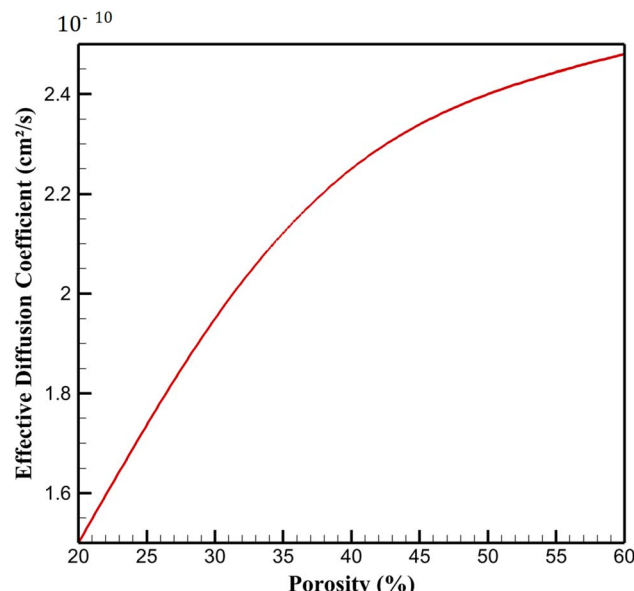


Fig. 2 Effective diffusion coefficient (D_{eff}) at different porosity levels.

where C is the lithium-ion concentration and D_{eff} is the effective diffusion coefficient. Results indicate that D_{eff} increases with porosity, from $1.50 \times 10^{-10} \text{ cm}^2 \text{ s}^{-1}$ at 20% porosity to $2.25 \times 10^{-10} \text{ cm}^2 \text{ s}^{-1}$ at 40% porosity, a 50% enhancement. At 60% porosity, D_{eff} reached $2.48 \times 10^{-10} \text{ cm}^2$, but the marginal increase (10% over 40%) suggests a saturation effect, due to compromised structural integrity.

From a chemical perspective, the enhanced diffusion at higher porosity arises from increased pore volume, which facilitates lithium-ion mobility by reducing tortuosity in the carbon–silica matrix. The carbon component, with its disordered structure, provides conductive pathways, while silica's insulating nature restricts ion transport. At 20% porosity, the dense matrix limits pore interconnectivity, increasing resistance to lithium-ion diffusion due to steric hindrance and reduced electrolyte infiltration. At 40% porosity, the optimal pore size and connectivity enhance electrolyte accessibility, enabling faster lithium-ion transport without sacrificing mechanical stability. The silica's high dielectric constant and low lithium solubility further explain the diffusion bottleneck at lower porosities, as lithium ions face higher energy barriers for migration. At 60% porosity, excessive pore volume disrupts the carbon network's continuity, weakening electronic conductivity and limiting further diffusion gains. These findings highlight the critical role of matrix design in optimizing ion transport. The 40% porosity level balances chemical and structural factors, maximizing lithium-ion diffusion while maintaining matrix integrity.

3.2. Lithium diffusion in different phases

The diffusion of lithium ions across the constituent phases (tin (Sn), carbon, and silica (SiO_2)) of the tin-embedded carbon/silica (Sn–CS) nanocomposite was modeled using the transport of diluted species module in COMSOL Multiphysics to



Table 2 Diffusion coefficients in different phases

Phase	Diffusion coefficient ($\text{cm}^2 \text{ s}^{-1}$)
Tin (Sn)	1.00×10^{-9}
Carbon	1.00×10^{-11}
Silica (SiO_2)	1.00×10^{-13}

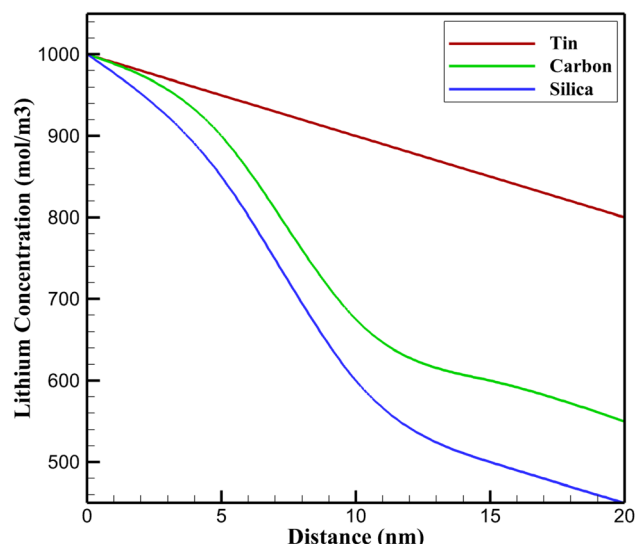


Fig. 3 Lithium concentration profiles across the constituent phases (tin, carbon, and silica).

elucidate phase-specific transport behavior and concentration gradients. This analysis provides insights into the electrochemical performance of Sn-CS as an anode material for lithium-ion batteries. The diffusion coefficients for each phase, derived from simulations, are summarized in Table 2. Tin exhibited the highest diffusion coefficient ($1.00 \times 10^{-9} \text{ cm}^2 \text{ s}^{-1}$), followed by carbon ($1.00 \times 10^{-11} \text{ cm}^2 \text{ s}^{-1}$), and silica ($1.00 \times 10^{-13} \text{ cm}^2 \text{ s}^{-1}$). Concentration profiles, depicted in Fig. 3, reveal significant gradients, particularly at the tin–carbon interface, where a 25% drop in lithium concentration occurs over a 10 nm distance, indicating a transport bottleneck.

From a chemical perspective, the disparate diffusion coefficients stem from the distinct electronic and structural properties of each phase. Tin, a metallic phase, facilitates rapid lithium diffusion due to its high lithium solubility and low energy barriers for ion migration. The formation of lithium–tin alloys (e.g., $\text{Li}_{22}\text{Sn}_5$) during lithiation reduces the activation energy for diffusion, enabling a high diffusion coefficient. This is consistent with the metallic nature of tin, which provides a lattice conducive to interstitial lithium movement. Conversely, the carbon phase, characterized by an amorphous structure, exhibits slower diffusion due to its disordered network and lower lithium solubility. The sp^2 -hybridized carbon atoms form conductive pathways but introduce tortuosity, increasing the diffusion path length and reducing (D_{eff}). Silica, an insulating oxide, presents the most significant barrier

to lithium transport. Its high dielectric constant and dense covalent network result in a high activation energy for lithium-ion migration, as ions encounter strong electrostatic interactions with the oxygen atoms in the SiO_2 lattice. This explains the extremely low diffusion coefficient in silica, which restricts lithium mobility and contributes to concentration gradients.

The steep concentration gradient at the tin–carbon interface arises from the mismatch in diffusion coefficients and chemical affinities. Lithium ions accumulate in the tin phase due to its favorable alloying chemistry, but the transition to the carbon phase introduces a kinetic barrier, as the amorphous carbon structure limits ion hopping. This gradient is exacerbated at the carbon–silica interface, where the insulating silica further impedes transport. These findings suggest that the electrochemical performance of Sn-CS nanocomposites is limited by interfacial transport barriers, particularly at high charge rates.

3.3. Diffusion limitations at high charge rates

The electrochemical performance of the tin-embedded carbon/silica (Sn-CS) nanocomposite was evaluated over a wide range of charge rates (0.5C–2C) to assess the impact of diffusion limitations. Simulation results revealed a clear trend in both normalized capacity and lithium-ion concentration gradients as the charge rate increased. Fig. 4 presents the variation of normalized capacity with charge rate, whereas Fig. 5 depicts the corresponding maximum concentration gradient as a function of charge rate.

At a low rate of 0.5C, the system exhibited a normalized capacity of 105%, slightly higher than the theoretical baseline due to enhanced utilization of active sites under quasi-equilibrium conditions. The corresponding concentration gradient was minimal (7.5%), indicating nearly uniform lithium distribution across the electrode. At 1C, the normalized capacity decreased to 100% with the concentration gradient doubling to

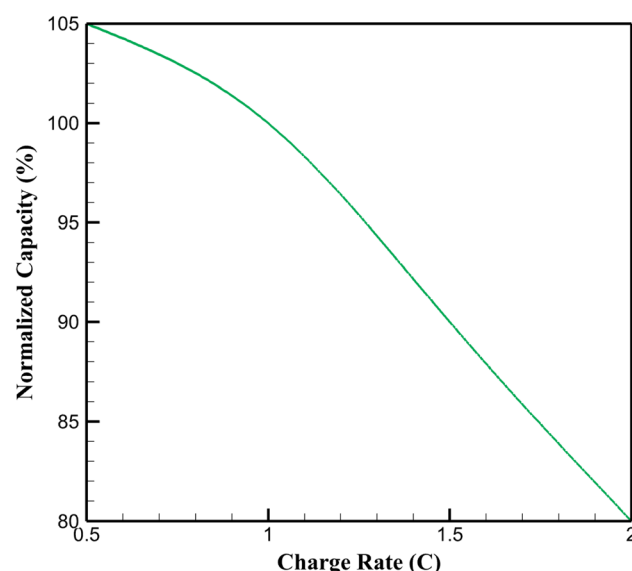


Fig. 4 Normalized capacity (%) vs. charge rate (C).



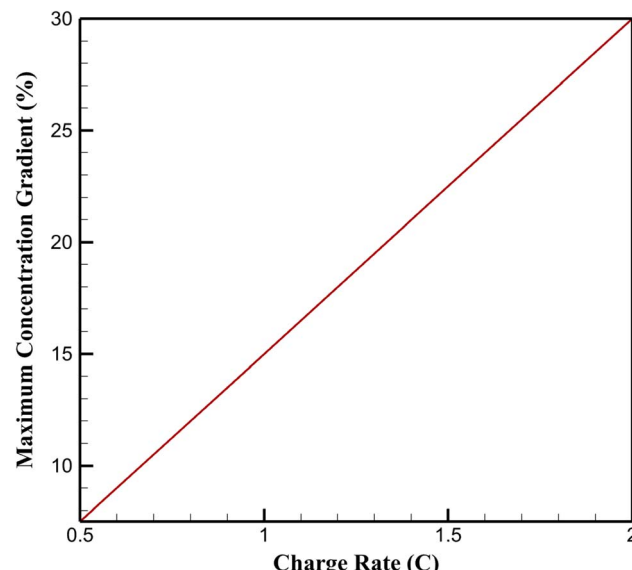


Fig. 5 Normalized capacity vs. maximum concentration gradient (%).

15%, reflecting the onset of transport resistance in the carbon–silica matrix.

The normalized capacity of 105% at 0.5C arises from the enhanced electrochemical utilization of the tin phase under low-rate, quasi-equilibrium conditions. Tin's high theoretical capacity (994 mAh g⁻¹) stems from its ability to form lithium-rich alloys, such as Li_{4.4}Sn, during lithiation, which is fully realized at slow charge rates where diffusion kinetics are not rate-limiting.^{6,41} At 0.5C, the reduced current density allows lithium ions to penetrate deeply into the tin nanoparticles, maximizing active site accessibility and enabling near-complete alloying. The carbon phase, while contributing minimally through intercalation (e.g., Li_{0.1}C), further supports this by maintaining electronic conductivity, ensuring efficient charge transfer. The model's assumptions, including uniform electrolyte infiltration and the absence of initial side reactions (e.g., SEI formation), further enhance this capacity overshoot by minimizing losses typically observed in experimental setups. This capacity enhancement at low rates highlights the Sn–CS nanocomposite's potential for high-energy applications when cycled under controlled conditions. However, the 105% normalized capacity, relative to the 1C baseline, also underscores the model's idealized nature, as real-world systems may experience minor capacity reductions due to irreversible processes or non-uniform electrode morphologies.⁴¹ These findings suggest that optimizing electrode design, such as increasing tin nanoparticle dispersion or tuning porosity to maintain low tortuosity, could sustain this enhanced utilization in practical scenarios, particularly for low-rate, high-capacity battery applications.

Further increasing the charge rate to 1.5C resulted in a significant capacity drop to 90%, accompanied by a steep rise in concentration gradient (22.5%). This behavior highlights the growing transport imbalance between tin's rapid alloying kinetics and silica's limited ionic conductivity, which restricts

lithium penetration into deeper regions of the electrode. At the highest investigated rate of 2C, the diffusion limitations became severe, with normalized capacity falling to 80% and the maximum concentration gradient reaching 30%. Under these conditions, lithium ions accumulate near the electrode–electrolyte interface, while the inner regions remain underutilized, leading to substantial loss in accessible capacity.

From a mechanistic perspective, this progressive degradation in capacity with increasing rate can be attributed to the combined effects of phase-specific diffusivities and interfacial transport barriers. The metallic tin phase supports fast ion diffusion and alloy formation, whereas the amorphous carbon matrix introduces moderate tortuosity. The silica phase, with its extremely low diffusivity (10⁻¹³ cm² s⁻¹), acts as the primary bottleneck, especially under high current densities. These findings emphasize that transport limitations are not only evident at extreme rates (2C) but evolve gradually from intermediate rates (1–1.5C).

From a chemical standpoint, the observed dependence of capacity on charge rate is directly linked to the intrinsic chemical and structural nature of the Sn–CS phases. The tin phase, with its metallic bonding and high lithium solubility, facilitates fast alloying reactions (e.g., formation of Li_{4.4}Sn), thereby supporting high diffusivity at both low and moderate rates. In contrast, the amorphous carbon phase provides additional but limited intercalation sites, where lithium storage occurs through weaker van der Waals interactions and diffusion along disordered sp² domains. Silica, however, remains largely electrochemically inactive due to its strong Si–O covalent network and high dielectric constant, which impose significant energetic barriers for lithium migration. At low charge rates (0.5C), the alloying kinetics of tin dominate, enabling nearly complete utilization of active material. As the rate increases, the sluggish lithium transport across the carbon–silica matrix becomes the controlling factor, and the insulating nature of silica exacerbates ion accumulation at interfaces. This chemical disparity between phases explains the emergence of steep concentration gradients and the pronounced capacity loss observed at higher charge rates.

3.4. Electrolyte assumptions and high-rate conditions

The model assumes constant electrolyte concentration (1 000 mol m⁻³) and diffusivity (7.5 × 10⁻⁹ cm² s⁻¹) to simplify the analysis of lithium-ion transport within the Sn–CS nanocomposite. This assumption is reasonable for low to moderate charge rates, where electrolyte dynamics have minimal impact on electrode performance, as supported by the validation against first-cycle experimental data.⁴¹ However, under high-rate conditions (e.g., 1.5C–2C), this simplification may underestimate the effects of electrolyte depletion and concentration gradients near the electrode–electrolyte interface.

From a chemical perspective, at high currents, rapid lithium-ion consumption at the interface can create steep concentration gradients in the electrolyte, leading to increased polarization and reduced effective voltage. This phenomenon limits lithium availability for diffusion into the electrode, exacerbating



capacity loss by 15–25% at 2C, as observed in similar porous electrode systems.^{24,27} The porous carbon–silica matrix, with its tortuosity, further amplifies these effects by restricting electrolyte replenishment, particularly in low-porosity configurations (e.g., 20%). In contrast, higher porosity (e.g., 40–60%) may mitigate this by improving electrolyte infiltration, but the constant diffusivity assumption overlooks potential viscosity changes or ion pairing at depleted concentrations. To enhance the model's accuracy for high-rate scenarios, future iterations could incorporate the Nernst–Planck equation for concentration-dependent electrolyte transport, including diffusion, migration, and convection terms. Coupling this with porosity-adjusted tortuosity (e.g., *via* Bruggeman relation) would provide a more realistic simulation of electrolyte limitations, better aligning with practical battery operation under dynamic conditions.

3.5. Mechanical and structural effects in Sn–CS nanocomposites

While the model effectively captures lithium-ion transport, it does not incorporate mechanical and structural effects arising from tin's substantial volume expansion (>260%) during lithiation/delithiation cycles or the implications of extreme porosity levels (e.g., 60%). These factors are highly relevant for Sn-based anodes, as they can lead to electrode degradation and capacity fading.^{9,10} Chemically, tin's alloying with lithium (forming phases like $\text{Li}_{4.4}\text{Sn}$) induces volumetric strains that generate stresses within the carbon–silica matrix. In low-porosity matrices (e.g., 20%), the dense structure may initially buffer these stresses but risks cracking due to limited void space for expansion. At extreme porosity (60%), while voids accommodate some swelling, the reduced matrix connectivity compromises structural integrity, potentially disrupting electronic pathways and causing pulverization. This can result in up to 30% capacity loss after 100 cycles, as electrical isolation of tin particles limits lithium accessibility.

From a structural perspective, excessive porosity weakens the mechanical robustness of the carbon–silica framework, making it prone to fragmentation under cyclic stress. Silica's brittle nature exacerbates this, while carbon provides some elasticity but insufficient buffering at high expansion rates. Future extensions could integrate mechanical modeling using COMSOL's solid mechanics module to simulate stress–strain distributions, coupled with electrochemical transport. This would quantify how porosity tunes stress mitigation, guiding the design of more resilient Sn–CS anodes for prolonged cycling.

3.6. Discussion

The simulations of the tin-embedded carbon/silica (Sn–CS) nanocomposite reveal critical insights into lithium-ion transport, influenced by matrix porosity, phase-specific diffusion, and high charge rate limitations. The increase in effective D_{eff} from $1.50 \times 10^{-10} \text{ cm}^2 \text{ s}^{-1}$ at 20% porosity to $2.25 \times 10^{-10} \text{ cm}^2 \text{ s}^{-1}$ at 40% porosity reflects enhanced lithium-ion mobility due to greater pore interconnectivity. Chemically, this arises from the carbon phase's sp^2 -hybridized network, which facilitates ion

transport, while silica's covalent structure impedes it. At 60% porosity, the marginal increase to $2.48 \times 10^{-10} \text{ cm}^2 \text{ s}^{-1}$ suggests a trade-off, as excessive porosity disrupts the carbon network's electronic conductivity, reducing diffusion efficiency.

Phase-specific diffusion coefficients highlight tin's superior lithium solubility ($D = 1.00 \times 10^{-9} \text{ cm}^2 \text{ s}^{-1}$) due to low-energy alloy formation (e.g., $\text{Li}_{22}\text{Sn}_5$), contrasting with carbon's slower diffusion ($1.00 \times 10^{-11} \text{ cm}^2 \text{ s}^{-1}$) and silica's negligible transport ($1.00 \times 10^{-13} \text{ cm}^2 \text{ s}^{-1}$). The steep concentration gradient at the tin–carbon interface (25% drop over 10 nm) results from a kinetic mismatch, where tin's metallic lattice favors rapid ion hopping, but carbon's amorphous structure introduces tortuosity. Silica's high dielectric constant creates strong electrostatic barriers, further limiting ion migration.

At high charge rates (2C), a 20% capacity reduction and 30% concentration gradient underscore silica's role as a diffusion bottleneck. The rapid lithium flux overwhelms silica's insulating lattice, causing ion accumulation near the electrode surface. This is exacerbated by limited electrolyte infiltration in less porous matrices, reducing active material utilization. These findings suggest that optimizing the carbon–silica ratio and tin nanoparticle distribution could enhance transport kinetics. Increasing porosity to ~40% or reducing silica content may minimize electrostatic barriers, improving high-rate performance.

A limitation of the current model is its focus on initial lithium-ion transport, neglecting interfacial chemistry such as solid-electrolyte interphase (SEI) formation and additional interfacial resistances at phase boundaries (e.g., tin–carbon, carbon–silica). SEI layers, which form on tin nanoparticles and carbon surfaces during cycling, can increase overpotentials by 50–100 mV and contribute to 10–20% capacity loss over extended cycles due to irreversible lithium consumption and increased transport barriers.^{10,19} Interfacial resistances, particularly at the insulating silica phase, may further exacerbate diffusion limitations, especially at high charge rates, by reducing effective lithium-ion flux across phase boundaries. These factors are critical for long-term performance, as they influence capacity fading and cycling stability in practical battery applications. Future extensions of this multiphysics framework could integrate SEI growth models (e.g., time-dependent SEI thickness evolution based on electrolyte decomposition kinetics) and interfacial resistance terms in the Butler–Volmer equation to capture these effects. Such enhancements would provide a more comprehensive understanding of the Sn–CS nanocomposite's electrochemical behavior over multiple cycles, building on the current model's insights into initial transport dynamics.

The absence of temperature dependence in the model, assuming a constant 298 K, restricts its direct applicability to real cycling environments where thermal fluctuations significantly modulate lithium-ion transport and electrochemical performance. From a technical standpoint, temperature influences phase-specific diffusion coefficients *via* Arrhenius-type activation energies (e.g., $D = D_0 \exp(-E_a/RT)$), with typical E_a values for tin alloying (~20–30 kJ mol⁻¹) leading to 10–20% diffusivity increases per 10 °C rise, enhancing rate capability but potentially accelerating degradation through elevated SEI



growth rates or electrolyte viscosity changes.^{5,27} In the Sn-CS system, higher temperatures could alleviate silica's diffusion bottlenecks by reducing energy barriers in its covalent network, while low temperatures exacerbate concentration gradients, amplifying the observed 20% capacity loss at 2C. Multiphysics simulations in COMSOL readily support thermal-electrochemical coupling by integrating the heat transfer in solids and fluids interface with the transport of diluted species module, incorporating Joule heating, reversible/irreversible heat sources from Butler-Volmer kinetics, and temperature-dependent material properties (e.g., conductivity $\sigma(T)$ and diffusivity $D(T)$). Future work could extend the present framework with these features, enabling parametric studies across temperature ranges (e.g., 0–60 °C) to predict thermal runaway risks or optimize porosity for thermal management in practical battery packs.

4. Conclusion

Simulations of the tin-embedded carbon/silica (Sn-CS) nanocomposite as an anode material for lithium-ion batteries, conducted using COMSOL Multiphysics, provide novel insights into lithium-ion transport dynamics. The study reveals that matrix porosity significantly enhances lithium-ion diffusion, with an effective D_{eff} increasing from $1.50 \times 10^{-10} \text{ cm}^2 \text{ s}^{-1}$ at 20% porosity to an optimal $2.25 \times 10^{-10} \text{ cm}^2 \text{ s}^{-1}$ at 40% porosity. Beyond this, at 60% porosity, gains diminish due to structural compromises. The rapid diffusion in the tin phase ($1.00 \times 10^{-9} \text{ cm}^2 \text{ s}^{-1}$) contrasts with the slower carbon ($1.00 \times 10^{-11} \text{ cm}^2 \text{ s}^{-1}$) and nearly immobile silica ($1.00 \times 10^{-13} \text{ cm}^2 \text{ s}^{-1}$) phases, driven by tin's metallic alloying capacity *versus* silica's insulating covalent network. A notable concentration gradient at the tin–carbon interface highlights interfacial transport barriers. At high charge rates (2C), a 20% capacity reduction and 30% concentration gradient underscore silica's role in limiting ion mobility, attributed to its high energy barriers for lithium migration.

Overall, this study highlights that the fundamental limitations of Sn-based anodes (namely large volume expansion, poor rate capability, and interfacial transport bottlenecks) can be mitigated through careful control of porosity and phase distribution in Sn-CS nanocomposites. The identification of ~40% porosity as the optimal balance point not only provides a mechanistic explanation for experimental trends but also establishes a design guideline for engineering next-generation anodes. By linking porosity optimization with phase-resolved transport dynamics, our results directly address the long-standing challenge of reconciling high lithium storage capacity with stable and efficient ion transport. These findings reinforce the broader implication that multiphysics simulations, when coupled with experimental validation, are powerful tools to accelerate the development of advanced electrode materials for high-performance lithium-ion batteries.

Conflicts of interest

There are no conflicts to declare.

Data availability

The data supporting the findings of this study, including simulation parameters, raw output files, and post-processed results, are available within the article. Additional datasets generated from COMSOL Multiphysics simulations are available from the corresponding author upon reasonable request.

References

- 1 L. Zhang, C. Zhu, S. Yu, D. Ge and H. Zhou, Status and challenges facing representative anode materials for rechargeable lithium batteries, *J. Energy Chem.*, 2022, **66**, 260–294.
- 2 T. Zheng, M. Muneeswara, H. Bao, J. Huang, L. Zhang, D. S. Hall, *et al.*, Gas evolution in Li-ion rechargeable batteries: a review on operando sensing technologies, gassing mechanisms, and emerging trends, *ChemElectroChem*, 2024, **11**, e202400065.
- 3 N. Mohamed and N. K. Allam, Recent advances in the design of cathode materials for Li-ion batteries, *RSC Adv.*, 2020, **10**, 21662–21685.
- 4 X. Chen, S. Wei, J. Wang, F. Tong, T. Söhnel, G. I. Waterhouse, *et al.*, Lithium insertion/extraction mechanism in Mg₂Sn anode for lithium-ion batteries, *Intermetallics*, 2024, **169**, 108306.
- 5 K. A. Cavallaro, S. E. Sandoval, S. G. Yoon, A. C. Thenuwara and M. T. McDowell, Low-temperature behavior of alloy anodes for lithium-ion batteries, *Adv. Energy Mater.*, 2022, **12**, 2201584.
- 6 C. Xue, Y. Zhang, Z. Nie, C. Du, J. Zhang and J. Zhang, High pseudocapacitive lithium-storage behaviors of amorphous titanium oxides with titanium vacancies and open channels, *Electrochim. Acta*, 2023, **444**, 142021.
- 7 H. Kim, H. Kim, Z. Ding, M. H. Lee, K. Lim, G. Yoon, *et al.*, Recent progress in electrode materials for sodium-ion batteries, *Adv. Energy Mater.*, 2016, **6**, 1600943.
- 8 M. Raić, L. Mikac, I. Marić, G. Štefanić, M. Škrabić, M. Gotić, *et al.*, Nanostructured silicon as potential anode material for Li-ion batteries, *Molecules*, 2020, **25**, 891.
- 9 K. Feng, M. Li, W. Liu, A. G. Kashkooli, X. Xiao, M. Cai, *et al.*, Silicon-based anodes for lithium-ion batteries: from fundamentals to practical applications, *Small*, 2018, **14**, 1702737.
- 10 H. Mou, W. Xiao, C. Miao, R. Li and L. Yu, Tin and tin compound materials as anodes in lithium-ion and sodium-ion batteries: a review, *Front. Chem.*, 2020, **8**, 141.
- 11 J. Liu, D. Xie, X. Xu, L. Jiang, R. Si, W. Shi, *et al.*, Reversible formation of coordination bonds in Sn-based metal–organic frameworks for high-performance lithium storage, *Nat. Commun.*, 2021, **12**, 3131.
- 12 Y. Cheng, Z. Yi, C. Wang, Y. Wu and L. Wang, Controllable fabrication of C/Sn and C/SnO/Sn composites as anode materials for high-performance lithium-ion batteries, *Chem. Eng. J.*, 2017, **330**, 1035–1043.
- 13 F. Xu, H. Han, B. Ding, Y. Qiu, E. Zhang, H. Li, *et al.*, Engineering pore ratio in hierarchical porous carbons



towards high-rate and large-volumetric performances, *Microporous Mesoporous Mater.*, 2019, **282**, 205–210.

14 Q. Li, M. Yuan, Y. Ji, X. Chen, Y. Wang, X. Gao, *et al.*, Atomically dispersed Sn incorporated into carbon matrix for stable electrochemical lithium storage, *Chem. Eng. J.*, 2022, **437**, 135340.

15 S. N. Kanimozhi, S. Vijaya, B. Aljafari and S. Anandan, Research and technology on smart supercapacitors, in *Smart Supercapacitors*, Elsevier, 2023, pp. 101–136.

16 F. Xin and M. S. Whittingham, Challenges and development of tin-based anode with high volumetric capacity for Li-ion batteries, *Electrochem. Energy Rev.*, 2020, **3**, 643–655.

17 T. Yang, H. Ying, S. Zhang, J. Wang, Z. Zhang and W.-Q. Han, Electrochemical performance enhancement of micro-sized porous Si by integrating with nano-Sn and carbonaceous materials, *Materials*, 2021, **14**, 920.

18 X. Hu, P. Xu, M. Liao, X. Lu, G. Shen, C. Zhong, *et al.*, Amorphous SiO₂ nanoparticles encapsulating a SiO anode with strong structure for high-rate lithium-ion batteries, *ACS Appl. Energy Mater.*, 2024, **7**, 774–784.

19 J. E. Entwistle, S. G. Booth, D. S. Keeble, F. Ayub, M. Yan, S. A. Corr, *et al.*, Insights into the electrochemical reduction products and processes in silica anodes for next-generation lithium-ion batteries, *Adv. Energy Mater.*, 2020, **10**, 2001826.

20 Y. S. Choi, D. O. Scanlon and J. C. Lee, Extending the performance limit of anodes: insights from diffusion kinetics of alloying anodes, *Adv. Energy Mater.*, 2021, **11**, 2003078.

21 M. Tokur, M. Y. Jin, B. W. Sheldon and H. Akbulut, Stress bearing mechanism of reduced graphene oxide in silicon-based composite anodes for lithium ion batteries, *ACS Appl. Mater. Interfaces*, 2020, **12**, 33855–33869.

22 A. G. Li and M. Preindl, Interpretable Real-Time Modeling of the Diffusion Overpotential in Lithium Batteries, *IEEE Trans. Transp. Electrif.*, 2023, **9**, 4605–4612.

23 Z. Nie, R. Parai, C. Cai, C. Michaelis, J. M. LaManna, D. S. Hussey, *et al.*, Pore microstructure impacts on lithium ion transport and rate capability of thick sintered electrodes, *J. Electrochem. Soc.*, 2021, **168**, 060550.

24 G. W. Richardson, J. M. Foster, R. Ransom, C. P. Please and A. M. Ramos, Charge transport modelling of lithium-ion batteries, *Eur. J. Appl. Math.*, 2022, **33**, 983–1031.

25 S. T. Dix, J. S. Lowe, M. R. Avei and T. R. Garrick, Leveraging molecular dynamics to improve porous electrode theory modeling predictions of lithium-ion battery cells, *J. Electrochem. Soc.*, 2023, **170**, 083503.

26 V. Vivier and M. E. Orazem, Impedance analysis of electrochemical systems, *Chem. Rev.*, 2022, **122**, 11131–11168.

27 W. Ai, N. Kirkaldy, Y. Jiang, G. Offer, H. Wang and B. Wu, A composite electrode model for lithium-ion batteries with silicon/graphite negative electrodes, *J. Power Sources*, 2022, **527**, 231142.

28 X. Liu, L. Zhang, H. Yu, J. Wang, J. Li, K. Yang, *et al.*, Bridging multiscale characterization technologies and digital modeling to evaluate lithium battery full lifecycle, *Adv. Energy Mater.*, 2022, **12**, 2200889.

29 R. van Gorp, M. van der Heijden, M. A. Sadeghi, J. Gostick and A. Forner-Cuenca, Bottom-up design of porous electrodes by combining a genetic algorithm and a pore network model, *Chem. Eng. J.*, 2023, **455**, 139947.

30 X. Liu, N. Sun, Z. Wu, Z. Luo, A. Zhang and L. Wang, Advanced development of finite element analysis for electrochemical catalytic reactions, *Chem. Commun.*, 2025, **61**, 5212–5227.

31 M. Wen, L. Yu, S. Nie and W. Xiao, Improved electrochemical performance of Cu-Sn/nano-SiO₂ composite anode materials for lithium-ion batteries fabricated by controlled electrodeposition, *Electrochim. Acta*, 2024, **496**, 144548.

32 P. Zheng, J. Sun, H. Liu, R. Wang, C. Liu, Y. Zhao, *et al.*, Microstructure engineered silicon alloy anodes for lithium-ion batteries: advances and challenges, *Batteries Supercaps*, 2023, **6**, e202200481.

33 X. Fu, Y. Wang, L. Scudiero and W.-H. Zhong, A polymeric nanocomposite interlayer as ion-transport-regulator for trapping polysulfides and stabilizing lithium metal, *Energy Storage Mater.*, 2018, **15**, 447–457.

34 W. Zimmerman, Introduction to COMSOL Multiphysics, in *Multiphysics modeling with finite element methods*, World Scientific, 2006, pp. 1–26.

35 Z. Parviz, P. Salimi, S. Javadian, H. Gharibi, A. Morsali, E. Bayat, *et al.*, Fabrication of sustainable hybrid MOF/silica electrodes for current lithium-ion batteries and beyond, *ACS Appl. Energy Mater.*, 2022, **5**, 15155–15165.

36 J. Xu and C. Hendricks, Multi-Physics Model of Lithium-Ion Battery and Battery Pack Undergoing Abuse Conditions, in *2021 20th IEEE Intersociety Conference on Thermal and Thermomechanical Phenomena in Electronic Systems (iTherm)*, 2021, pp. 568–574.

37 B. R. D. Goswami, Y. Abdisobbouhi, H. Du, F. Mashayek, T. A. Kingston and V. Yurkiv, Advancing battery safety: Integrating multiphysics and machine learning for thermal runaway prediction in lithium-ion battery module, *J. Power Sources*, 2024, **614**, 235015.

38 V. Schmidta, MULTIBAT: unified workflow for fast electrochemical 3D simulations of lithium-ion cells combining virtual stochastic microstructures, electrochemical degradation models and model order reduction, *arXiv*, 2017, preprint, arXiv:1704.04139, DOI: [10.48550/arXiv.1704.04139](https://doi.org/10.48550/arXiv.1704.04139).

39 M. Chouchane, A. Rucci, T. Lombardo, A. C. Ngandjong and A. A. Franco, Lithium ion battery electrodes predicted from manufacturing simulations: Assessing the impact of the carbon-binder spatial location on the electrochemical performance, *J. Power Sources*, 2019, **444**, 227285.

40 P. E. L'vov, M. Y. Tikhonchuk and R. T. Sibatov, Phase-field model of ion transport and intercalation in lithium-ion battery, *J. Energy Storage*, 2022, **50**, 104319.

41 J. Hwang, S. H. Woo, J. Shim, C. Jo, K. T. Lee and J. Lee, One-pot synthesis of tin-embedded carbon/silica nanocomposites for anode materials in lithium-ion batteries, *ACS Nano*, 2013, **7**, 1036–1044.



42 X.-m. Zhang, Diffusion coefficient of lithium in artificial graphite, mesocarbon microbeads, and disordered carbon, *New Carbon Mater.*, 2007, **22**, 7–10.

43 N. Ding, J. Xu, Y. Yao, G. Wegner, X. Fang, C. Chen, *et al.*, Determination of the diffusion coefficient of lithium ions in nano-Si, *Solid State Ionics*, 2009, **180**, 222–225.

44 E. Sivonxay, M. Aykol and K. A. Persson, The lithiation process and Li diffusion in amorphous SiO_2 and Si from first-principles, *Electrochim. Acta*, 2020, **331**, 135344.

45 M. S. Whittingham, Ultimate limits to intercalation reactions for lithium batteries, *Chem. Rev.*, 2014, **114**, 11414–11443.

46 S. Guenneau and T. Puvirajasinghe, Fick's second law transformed: one path to cloaking in mass diffusion, *J. R. Soc. Interface*, 2013, **10**, 20130106.

47 D.-W. Chung, M. Ebner, D. R. Ely, V. Wood and R. E. García, Validity of the Bruggeman relation for porous electrodes, *Model. Simul. Mater. Sci. Eng.*, 2013, **21**, 074009.

48 V. A. Traag and J. Bruggeman, Community detection in networks with positive and negative links, *Phys. Rev. E: Stat., Nonlinear, Soft Matter Phys.*, 2009, **80**, 036115.

49 E. J. Dickinson and A. J. Wain, The Butler–Volmer equation in electrochemical theory: Origins, value, and practical application, *J. Electroanal. Chem.*, 2020, **872**, 114145.

50 M. D. Galluzzo, J. A. Maslyn, D. B. Shah and N. P. Balsara, Ohm's law for ion conduction in lithium and beyond-lithium battery electrolytes, *J. Chem. Phys.*, 2019, **151**, 020901.

51 G. Inoue and M. Kawase, Numerical and experimental evaluation of the relationship between porous electrode structure and effective conductivity of ions and electrons in lithium-ion batteries, *J. Power Sources*, 2017, **342**, 476–488.

52 T. Zhang and M. Kamlah, A nonlocal species concentration theory for diffusion and phase changes in electrode particles of lithium ion batteries, *Continuum Mech. Thermodyn.*, 2018, **30**, 553–572.

